Gravity Waves in Idealized MM5 Simulations

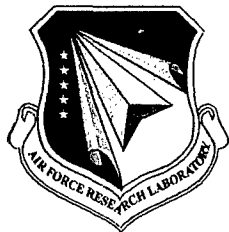Susan A. Triantafillou

Atmospheric and Environmental Research, Inc.
131 Hartwell Avenue
Lexington, MA 02421

Scientific Report No. 3

15 April 2006

APPROVED FOR PUBLIC RELEASE; DISTRIBUTION UNLIMITED.

AIR FORCE RESEARCH LABORATORY
Space Vehicles Directorate
29 Randolph Road
AIR FORCE MATERIEL COMMAND
Hanscom AFB, MA 01731-3010

20060816327

This technical report has been reviewed and is approved for publication.

AFRL-VS-HA-TR-2006-1066

/Signed/   /Signed/

EDMUND MURPHY   ROBERT BELAND, Chief
Contract Manager   Battlespace Surveillance Innovation Center

REPORT DOCUMENTATION PAGE

Form Approved
OMB No. 0704-0188

1. REPORT DATE (DD-MM-YYYY)	2. REPORT TYPE	3. DATES COVERED (From - To)
15-04-2006	Scientific Report No. 3	04-2004 To 04-2005

4. TITLE AND SUBTITLE	5a. CONTRACT NUMBER
Gravity Waves in Idealized MM5 Simulations	F19628-03-C-0038
	5b. GRANT NUMBER
	5c. PROGRAM ELEMENT NUMBER 69120C

6. AUTHOR(S)	5d. PROJECT NUMBER DOEA
Triantafillou, Susan A.	**5e. TASK NUMBER** OT
	5f. WORK UNIT NUMBER A1

7. PERFORMING ORGANIZATION NAME(S) AND ADDRESS(ES)	8. PERFORMING ORGANIZATION REPORT NUMBER
Atmospheric and Environmental Research, Inc. 131 Hartwell Avenue Lexington, MA 02421-3126	X0007-SR3-I-00Z

9. SPONSORING/MONITORING AGENCY NAME(S) AND ADDRESS(ES)	10. SPONSOR/MONITOR'S ACRONYM(S)
Air Force Research Laboratory 29 Randolph Road Hanscom AFB, MA 01731-3010	AFRL/VSBYM
	11. SPONSORING/MONITORING AGENCY REPORT NUMBER AFRL-VS-HA-TR-2006-1066

12. DISTRIBUTION AVAILABILITY STATEMENT

Approved for public release; distribution unlimited.

13. SUPPLEMENTARY NOTES

14. ABSTRACT
Propagation and dissipation of gravity waves in the NCAR/Penn State Mesoscale Model (MM5) are studied using numerical experiment, numerical analysis, and established theory. The waves, which are due to a small, fixed-frequency disturbance in an idealized atmosphere, form beams in an X-shaped pattern known as St. Andrew's Cross. This choice of problem is accompanied by a theory, supported by physical experiment, and it allows the MM5 wave propagation by the model's dynamical core to be distinguished from other model functions, such as boundary conditions or physics parameterizations. Gravity-wave theory predicts the amount of amplitude loss along the beams in a viscous, Boussinesq fluid. This is adapted for compressibility and used as a gauge for the dissipation due to the dynamical core of the MM5, in which dissipation is strictly numerical. Eight numerical experiment cases with various grid and wave parameters are simulated and measured in terms of amplitude loss. Results show amplitude losses among the eight cases can be greater or less than theory predicts for a viscous fluid, depending on parameter values. As expected, numerical dissipation decreases or increases with respectively finer or coarser resolution of gravity waves. This is confirmed by the numerical analysis, which also predicts sensitivity of MM5 dissipation for grid and wave parameters not specifically considered by the numerical experiments. Numerical dissipation is more sensitive to changes in horizontal parameters than vertical ones, reflecting the impact of artificial dissipation used in MM5's horizontal advection scheme. Comparison of experimental and theoretical results shows the experimental numerical dissipation matches that of molecular viscosity when approximately eleven horizontal grid cells represent one wave. These results are relevant to selection of MM5 grid spacing when wave behavior is expected and interpretation of MM5 forecast dependence on grid spacings.

15. SUBJECT TERMS
Gravity waves, Numerical dissipation, Mesoscale atmospheric model, Optical turbulence

16. SECURITY CLASSIFICATION OF:			17. LIMITATION OF ABSTRACT	18. NUMBER OF PAGES	19a. NAME OF RESPONSIBLE PERSON Edmund Murphy
a. REPORT Unclassified	b. ABSTRACT Unclassified	c. THIS PAGE Unclassified	U	34	19b. TELEPONE NUMBER (Include area code)

Contents

Figures

Tables

1 Introduction

This study is motivated by the need for better accuracy in atmospheric turbulence predictions for the upper troposphere and lower stratosphere based on the Penn State/NCAR Mesoscale Model Generation 5 (MM5) (Dudhia 1993; Grell et al. 1994). Although turbulence itself is not captured by the MM5, MM5-predicted atmospheric profiles of winds and temperatures are used as input into a turbulence parameterization, such as the Dewan model (Dewan et al. 1993), to calculate turbulence along paths on the order of 1000 km long, providing a feasible method for real-time turbulence predictions for use in aviation and military applications.

Field measurements of turbulence and other atmospheric quantities were made to assess the accuracy of such predictions and to compare them to turbulence parameterizations based on observed profiles (Ruggiero et al. 2004). This revealed cases where MM5-based predictions failed because of MM5 inaccuracies, characterized by vertical profiles in which high-resolution features were lacking or severely smoothed. This prompted the current assessment of impacts on MM5 accuracy as it pertains to atmospheric turbulence calculations. Gravity waves are of interest in this regard because gravity waves can create shear instabilities that produce turbulence.

Gravity waves are the focus of this study due to their association with turbulence. The MM5 captures gravity waves, but the model was developed as a weather-forecasting tool and its simulations are subject to numerical damping that was not optimized for gravity-wave forecasting. In the context of turbulence forecasting, damping of gravity waves is of interest, especially in consideration of the smoothed MM5 profiles in cases of inaccurate turbulence predictions.

Related research by Leutbecher and Volkert (2000) compared several MM5 simulations to an observed gravity-wave event induced by flow over a mountain. This showed how variations in horizontal grid spacing and surface friction values were important in determining the accuracy of the simulated wave amplitude. Horizontal grid spacing affected accuracy because it impacted the resolution of the mountain and the amount of artificial dissipation, which is targeted to control numerical instability of waves that are small relative to grid spacing. A result of the study was an optimal pairing of surface friction value and horizontal resolution (the finest) for the given wave event.

The present study aims to separate MM5 wave propagation by the model's dynamical core from other model functions and to generalize results to a range of gravity waves. The dynamical core refers to that part of the model that is adiabatic and invisid and thus mainly pertains to advection of conserved properties. That is, propagation is modeled without the parameterizations typically used to represent subgrid scale influences, and boundary layer processes so that the effects of the dynamical core are isolated. In our idealized simulation, conditions at one boundary correspond to gravity waves entering the model domain. Then calculated values along the center of the propagating gravity wave are used to evaluate how the amplitude of the wave evolves. The problem simulated has an analytical solution so the observed loss in wave amplitude can be assessed in terms of theoretical results. Further to

1

generalize the simulation results we conduct a numerical analysis of the linear behavior of the discretized model equations.

The problem simulated is the two-dimensional gravity-wave problem characterized by the X-shaped wave pattern, known as St. Andrew's cross, shown in the photographs by Mowbray and Rarity (1967). A density-stratified fluid with constant Brunt Väisällä frequency, initially at rest, is disturbed by an oscillator, which results in four straight gravity-wave beams propagating from the disturbance location and forming an X pattern. The nonlinear problem is solved analytically by Tabaei and Akylas (2003) for a two-dimensional, viscous, Boussinesq fluid. They show that after initial transients died out, their solution corresponds to the solution of Thomas and Stevenson (1972) who validate the solution with experimental measurements. It turns out that in the inviscid case, the nonlinear and linear solutions are identical and prescribe a uniform fluid speed along each beam center. Tabaei and Akylas showed how the presence of viscosity causes the beam-center speed to decrease as the beam propagates away from the disturbance.

For the MM5 simulation of St. Andrew's cross, moisture, rotation, and other effects that are important in the real atmosphere are eliminated, making model conditions close to those of the Tabaei and Akylas (2003) solution. The compressibility in the model must be retained and therefore, the theoretical Boussinesq results for the beam-center speed are adapted to a compressible fluid for comparison to model results. Although both the model and theory are nonlinear, small disturbances are used here to generate a linear response for consistency with numerical analysis described later. Results from eight model runs, reflecting different grid sizes and wavelengths, are compared to the theoretical prediction for loss in beam amplitude. This shows MM5 losses can be greater or less than predictions, depending on grid and wave parameters.

A linear analysis is used explore the sensitivity of the MM5's numerical dissipation to changes in grid and wave parameters. It is noted that the damping in the MM5 is strictly numerical, as real viscosity is not explicitly simulated by the dynamical core of the model. The MM5 is a fully compressible, nonhydrostatic, three-dimensional model. Variables are updated using a combination of explicit time stepping with artificial dissipation for horizontal momentum equations and implicit time stepping for vertical momentum and entropy equations. The terms in all equations are partitioned into fast-changing terms, which are updated on small time steps, and slowly-changing terms, which are updated on large time steps.

Numerical experiments result in observed amplitude changes that vary with grid and wave parameters. The observed values show how numerical dissipation in the MM5 dynamical core compares to the dissipation that would be present with molecular viscosity. Numerical dissipation is decreased with finer wave resolution in either the horizontal or vertical, with greater sensitivity to horizontal resolution. This is supported by both numerical experiments and numerical analysis. Numerical analysis is used to calculate amplitudes for a range of horizontal and vertical parameters, showing these sensitivities.

2 Theory

The relevant equations and their analytical solution are discussed here and used in the next section where the numerical method is analyzed. The two-dimensional conservation equations of continuity, momentum, and entropy are taken for a compressible, inviscid, adiabatic, ideal gas and linearized about a motionless background state with constant Brunt Väisällä frequency and temperature. Although approximate solutions adequately describe gravity waves for many purposes, the compressible case is most relevant since compressibility is an essential feature of the MM5 numerical method. This problem leads to a gravity-wave solution and the associated dispersion relation. When the problem is further simplified using the Boussinesq approximation, a gravity-wave beam solution is obtained. It is shown by Tabaei and Akylas that the Boussinesq solution for the linearized problem is the same as that for the nonlinear problem. Furthermore, they give the solution for the Boussinesq case with viscosity. All of these solutions are considered here.

The perfect gas law,

$$\tilde{p} = \tilde{\rho} R \tilde{T} \tag{1}$$

where $\tilde{p}$, $\tilde{\rho}$, and $\tilde{T}$ are pressure, density, and temperature, respectively, and where R is the gas constant for air, is linearized using the sum of a background state quantity, indicated by the subscript 0, and a perturbation quantity,

$$\tilde{p} = p_0 + p + \cdots, \quad \tilde{\rho} = \rho_0 + \rho + \cdots \quad \text{and} \quad \tilde{T} = T_0 + T + \cdots. \tag{2}$$

Requiring that Equation (1) holds for the background quantities and ignoring terms of second order leads to the linearized perfect gas equations,

$$p = \rho_0 T R + \rho T_0 R. \tag{3}$$

Since it is already linear the hydrostatic relationship for the perturbation quantities

$$\frac{\partial p}{\partial z} = -\rho g \tag{4}$$

has the same form as for the full and background variables.

The background state sound speed, c_0, and Brunt Väisällä frequency, N, are constants in this treatment, given by

$$c_0^2 = \gamma R T_0, \quad \text{and} \quad N = \frac{g}{c_0}\sqrt{\gamma - 1}, \tag{5}$$

where γ is the ratio of the specific heat of dry air at constant pressure to the specific heat of dry air at constant volume and g is the gravitational constant.

In preparation for the numerical analysis, the governing equations are shown in the form used in the MM5 and without the added damping terms from the MM5. The momentum,

pressure, and temperature equations are

$$\frac{\partial u}{\partial t} + \frac{1}{\rho_0}\frac{\partial p}{\partial x} = 0, \tag{6}$$

$$\frac{\partial w}{\partial t} + \frac{1}{\rho_0}\frac{\partial p}{\partial z} = -g\frac{\rho}{\rho_0}, \tag{7}$$

$$\frac{\partial p}{\partial t} + \rho_0 c_0^2 \delta - \rho_0 g w = 0, \tag{8}$$

$$\frac{\partial T}{\partial t} = \frac{1}{\rho_0 c_p}\frac{\partial p}{\partial t} - \frac{g}{c_p}w, \tag{9}$$

$$\delta = \frac{\partial u}{\partial x} + \frac{\partial w}{\partial z}. \tag{10}$$

Equations (6) - (10) match those shown in Grell et al. (1994, referred to hereafter as G94), when the MM5 mapping factor is $m = 1$, the reference pressure p^* is constant (as it would be for flat terrain), and using z as a vertical coordinate. Specifically, Equations (6) - (9) above can be obtained respectively from Equations (2.2.1) or (2.5.1.1), Equations (2.2.3) or (2.5.1.3), Equation (2.2.4), and Equation (2.2.5) in G94.

Equations (6) - (10) are equivalent to those presented in Lighthill (1978) for the flow of an inviscid, linearized, compressible, constant N fluid. The momentum equations above, Equations (6) and (7), are both represented by the (vector) Equation (16) in Lighthill's Section 4.1. The pressure equation, Equation (8) above, can be obtained by combining Lighthill's equation for a reversible process, or Equation (33) in Section 4.1, with the continuity equation, or Equation (30) from Section 4.1. The temperature equation, Equation (9) above, can be derived from Equation (33) in Lighthill Section 4.1, along with the linearized perfect gas law, the hydrostatic relation, and the relations between constants in Equation (5). Thus, the solution from Lighthill applies here.

The solution to Equations (6) - (10) takes the form

$$\rho = \mathcal{R}\exp(i\phi), \quad \rho_0 u = \mathcal{U}\exp(i\phi), \quad \rho_0 w = \mathcal{W}\exp(i\phi), \quad p = \mathcal{P}\exp(i\phi), \tag{11}$$

where

$$\phi = k_x x + k_z z - \omega t, \tag{12}$$

ω is the temporal frequency, and k_x and k_z are the spatial frequencies in the x- and z-dimensions, respectively. This leads to the dispersion relation

$$\frac{\omega^4}{c_0^2} - \left[k_x^2 + k_z^2 - ik_z\frac{\gamma N^2}{(\gamma - 1)g}\right]\omega^2 + k_x^2 N^2 = 0, \tag{13}$$

as shown in Lighthill (1978). Provided that the background density varies slowly over the length of a gravity wave, the approximate dispersion relation is

$$\omega^2 = \frac{N^2 k_x^2}{k_x^2 + k_z^2}, \tag{14}$$

4

which coincides with the Boussinesq dispersion relation. The wave-dependent coefficients in (11) are related by

$$\frac{\mathcal{P}}{\mathcal{U}} = \frac{\omega}{k_x}, \quad \frac{\mathcal{P}}{\mathcal{W}} = \frac{N^2 - \omega^2}{\omega \left(ig\frac{1}{c_0^2} - k_z \right)}, \quad \frac{\mathcal{R}}{\mathcal{W}} = \frac{i\omega}{g} - \frac{ik_z}{g}\frac{\mathcal{P}}{\mathcal{W}}. \tag{15}$$

The nonlinear, two-dimensional, Boussinesq beam problem was solved by Tabaei and Akylas (2003) for a stably stratified fluid with background density, ρ_0, that varies exponentially with height. The gravity-wave dispersion relation, which coincides with the linear case, is

$$(\omega/N)^2 = \sin^2\theta, \tag{16}$$

where θ, the wave propagation angle in the x–z plane, is defined by

$$(k_x, k_z) = K(\sin\theta, -\cos\theta). \tag{17}$$

Wave groups move with the group velocity given by

$$\mathbf{C}_g = \frac{N\cos\theta}{K}(\cos\theta, \sin\theta). \tag{18}$$

Provided

$$k_z \gg -\frac{\rho_0'}{\rho_0}, \tag{19}$$

these results are a good approximation to the linear, compressible solution, which is presented later and can be found in Lighthill (1978).

Along the center of a beam, the fluid speed is constant for the inviscid, Boussinesq case. Tabaei and Akylas (2003) showed that when viscosity is accounted for, beam-center speed, V, away from the disturbance decays according to

$$V \propto \frac{1}{|\xi|^{2/3}}, \tag{20}$$

where ξ is the beam-following coordinate,

$$\xi = x\cos\theta + z\sin\theta. \tag{21}$$

The beam amplitude prediction is reinterpreted here for a compressible fluid, for consistency with MM5 assumptions. In a compressible fluid, the factor of $\sqrt{\rho_0}$ constitutes the leading correction to Boussinesq results (Lighthill 1978). Therefore, the beam amplitude in the compressible, viscous case used here is

$$V\sqrt{\rho_0} \propto \frac{1}{|\xi|^{2/3}}. \tag{22}$$

This amplitude prediction is used to gauge whether MM5 beam amplitudes are diminished by MM5 damping more or less than they would be by molecular viscosity.

5

3 Numerical Analysis

To examine how damping of gravity waves in MM5 varies with grid and wave parameters, the discrete forms of (6) - (9) are analyzed using the MM5 numerical scheme. Many of the techniques used here are shown in Durran (1999). A result is a numerical dispersion relation from which the wave frequency and the wave amplification factor are found.

The MM5 numerical scheme is based on a form of Equations (6) - (10) with added damping and averaging to accommodate the staggered grid. The equations are rewritten with these features and using $R = c_p - c_v$, $\gamma = c_p/c_v$, and $c_o^2 = \gamma p_0/\rho_0$. The result, after some rearrangment, is

$$\frac{\partial u}{\partial t} + c_0 \frac{\partial}{\partial x}\left(\frac{p}{\rho_0 c_0}\right) - \alpha_x \frac{\partial \delta}{\partial x} = D(u), \tag{23}$$

$$\frac{\partial w}{\partial t} + c_0 \frac{\partial}{\partial z}\left(\frac{p}{\rho_0 c_0}\right) + \frac{g}{c_0}\overline{\left(\frac{p}{\rho_0 c_0}\right)} = \frac{g(\gamma - 1)}{c_0}\left(\frac{c_p T}{c_0} - \frac{p}{\rho_0 c_0}\right) + D(w), \tag{24}$$

$$\frac{\partial}{\partial t}\left(\frac{p}{\rho_0 c_0}\right) + c_0 \delta - \frac{g}{c_0}\overline{w} = 0, \tag{25}$$

$$\frac{\partial}{\partial t}\left(\frac{c_p T}{c_0}\right) = \frac{\partial}{\partial t}\left(\frac{p}{\rho_0 c_0}\right) - \frac{g}{c_0}\overline{w} - D\left(\frac{p}{\rho_0 c_0}\right) + D\left(\frac{c_p T}{c_0}\right), \tag{26}$$

where the D terms are fourth order diffusion terms, the α term is divergence damping, and the overbar indicates vertical averaging. The damping terms are used in MM5 for numerical stability and do not reflect a physical process.

The vertical coordinate, z, used here differs from the pressure-based coordinate used in the MM5, since use of the MM5 coordinate would unnecessarily complicate the analysis. For the given base state the results would not change since pressure levels and z levels coincide. In the MM5 simulations the pressure levels are chosen to correspond to equal increments in z.

The MM5 equations, approximated by the linearized equations in (23) - (26) with (10), are discretized with centered differences in space. Note in what follows that the MM5 staggers the grids of the different variables. In the horizontal domain the Arakawa D grid is used in which the thermodynamical variables (temperature and moisture) and vertical velocity are defined at the full grid points (with integer indices) and the horizontal wind components are defined at the half grid points, $i.e.$, at the corners of the grid boxes centered on the full grid points. In the vertical, vertical velocity is defined at the full grid points and all other variables are defined at the half grid points. Therefore, the first derivatives of a variable, v, accounting for grid staggering, are approximated in the MM5 by

$$\frac{\partial v}{\partial x} \approx \frac{v_{j+1/2} - v_{j-1/2}}{x_{j+1/2} - x_{j-1/2}} \quad \text{and} \quad \frac{\partial v}{\partial z} \approx \frac{v_{k+1/2} - v_{k-1/2}}{z_{k+1/2} - z_{k-1/2}}, \tag{27}$$

and the vertical average is

$$\overline{v} = \frac{v_{k+1/2} + v_{k-1/2}}{2}. \tag{28}$$

6

For a wave mode represented by

$$v = V \exp\left(ik_x x + ik_z z\right) \exp\left(-i\omega t\right) \tag{29}$$

and using $\Delta x = x_{j+1/2} - x_{j-1/2}$ and $\Delta z = z_{k+1/2} - z_{k-1/2}$, the approximate derivatives and the vertical average can be written,

$$\frac{\partial v}{\partial x} \approx \partial_x v = \frac{i \sin k_x \Delta x/2}{\Delta x/2} v, \tag{30}$$

$$\frac{\partial v}{\partial z} \approx \partial_z v = \frac{i \sin k_z \Delta z/2}{\Delta z/2} v, \tag{31}$$

$$\overline{v} = a_z v = \cos k_z \Delta z/2 \, v. \tag{32}$$

An artificial fourth order diffusion is included in the MM5 to selectively dissipate the smallest scale waves. Otherwise, because of aliasing, significant energy would accumulate in these scales. The fourth order diffusion terms are defined so that $D(v)$ approximates $D_4 \partial^4 v / \partial x^4$, with D_4 a constant dependent on grid parameters. This approximation is accomplished by

$$D(v) = D_4 \frac{v_{j+2} - 4v_{j+1} + 6v_j - 4v_{j-1} - v_{j-2}}{\Delta x^4}, \tag{33}$$

$$D_4 \approx .003 \frac{\Delta x^4}{\Delta \tau}, \tag{34}$$

where the D_4 value is approximated using Section 5.1 in G94, recognizing that the MM5 coefficient called K_H is dominated by the K_{H0} contribution for gravity waves and $\Delta \tau$ is the so-called small time step. Using the wave mode given above, the fourth order diffusion term is

$$D(v) = D_x v = -\frac{.012}{\Delta \tau} \left(\cos k_x \Delta x - 1\right)^2 v. \tag{35}$$

Discretizing the spatial derivatives and using the above notation for averages, Equations (23) - (26) and (10) are written in differential-difference form as

$$\frac{\partial u}{\partial t} + c_0 \partial_x \left(\frac{p}{\rho_0 c_0}\right) - \alpha_x \partial_x \delta = D_x u, \tag{36}$$

$$\frac{\partial w}{\partial t} + c_0 \partial_z \left(\frac{p}{\rho_0 c_0}\right) + \frac{g}{c_0} \overline{\left(\frac{p}{\rho_0 c_0}\right)} = \frac{g(\gamma - 1)}{c_0} \left(\frac{c_p T}{c_0} - \frac{p}{\rho_0 c_0}\right) + D_x w, \tag{37}$$

$$\frac{\partial}{\partial t} \left(\frac{p}{\rho_0 c_0}\right) + c_0 \delta - \frac{g}{c_0} \overline{w} = 0, \tag{38}$$

$$\frac{\partial}{\partial t} \left(\frac{c_p T}{c_0}\right) = \frac{\partial}{\partial t} \left(\frac{p}{\rho_0 c_0}\right) - \frac{g}{c_0} \overline{w} - D_x \frac{p}{\rho_0 c_0} + D_x \frac{c_p T}{c_0}, \tag{39}$$

where δ is now interpreted in terms of the difference notation so

$$\delta = \partial_x u + \partial_z w. \tag{40}$$

7

The above equations are next subject to the time differencing for the time derivatives, and time-level assignments for all variables. In summary, the MM5 scheme partitions terms in the momentum and pressure equations into fast-changing, or acoustic, terms and slowly changing terms. The fast-changing terms are updated on small time steps, $\Delta\tau$, while the slowly-changing terms are updated on large time steps, $2\Delta t$. In addition, some of the slowly-changing terms are updated at times $t - \Delta t$, $t + \Delta t$, etc., while others are updated at times, t, $t + 2\Delta t$. So at any given time step, multiple time levels must be represented. The scheme is described in more detail below and used to rewrite the differential-difference equations as difference-only equations. This combination of split-explicit and odd/even centered (or "leap frog") time steps, along with a time filter to keep the odd and even solutions from diverging, is used in MM5 to simultaneously optimize the efficiency and accuracy of the model.

The fast-changing terms in the MM5 appear on the left hand side of (36) - (38) and slowly-changing terms appear on the right hand side. The slowly-changing terms in the vertical momentum equation (37) are individually susceptible to acoustic oscillations, but their sum is equivalent to the slowly-varying potential temperature term, $\rho_0 g \Theta/\Theta_0$, where Θ_0 and Θ are the leading terms in the expanded potential temperature and $\Theta_0 = p_0/(\rho_0 R)(p_s/p_0)^{(\gamma-1/\gamma)}$, with a reference pressure p_s.

The acoustic terms, which appear on the left hand side of (36) - (38), are updated at every small time step, $\Delta\tau$, while the other terms are updated on large, "leap frog" (*i.e.*, centered) time steps of size $2\Delta t$, with $4\Delta\tau = 2\Delta t$, typically. The small time steps involve stepping forward in time, so that for u for example,

$$\frac{\partial u}{\partial t} \approx \frac{u(\tau + \Delta\tau) - u(\tau)}{\Delta\tau}, \tag{41}$$

and likewise for w and $p/(\rho_0 c_0)$. In MM5 the u equation is stepped forward explicitly and then the updated u values are used in the w and $p/(\rho_0 c_0)$ equations. Equations (37) and (38) are made implicit in the small time steps by using time-averaged values for pressure and vertical velocity. As described in Section 2.5.1 in G94, occurences of $p/(\rho_0 c_0)$ among the fast-changing terms in the w equation, or on the right hand side of Equation (37), are replaced by the time-averaged value

$$\frac{1+\beta}{2} \frac{p}{\rho_0 c_0}(\tau + \Delta\tau) + \frac{1-\beta}{2} \frac{p}{\rho_0 c_0}(\tau), \tag{42}$$

where $0.2 < \beta < 0.4$. Similarly, occurences of w on the right hand side of Equation (38) are replaced by the analogous time averaged value of w. For analysis purposes the median value $\beta = 0.3$ is adopted.

The temperature is updated on leap frog steps, which leap from $t - \Delta t$ to $t + \Delta t$. The nonacoustic terms, other than the fourth order diffusion terms, are evaluated at the large time levels in between these leaps, or t, $t + 2\Delta t$, etc. The fourth order diffusion terms are evaluated at $t - \Delta t$, $t + \Delta t$, etc. To write the difference equations, time-level superscripts are used, with m and n superscripts representing small and large time steps, respectively.

8

The small-step difference in (41) is written

$$\frac{u(\tau + \Delta\tau) - u(\tau)}{\Delta\tau} = \frac{u^{m+1} - u^m}{\Delta\tau}, \tag{43}$$

while the large-step difference to approximate the time derivatives in Equation (39) use the form,

$$\frac{\frac{c_p}{c_0}T^{n+1} - \frac{c_p}{c_0}T^{n-1}}{\Delta t}. \tag{44}$$

Starting from the step $n - 1 = m$, the first small time step gives the difference equations

$$u^{m+1} = u^m \tag{45}$$
$$+\Delta\tau\left[-c_0\partial_x\left(\frac{p}{\rho_0 c_0}\right)^m + \alpha_x\partial_x(\partial_x u^m + \partial_z w^m) + D_x u^{n-1}\right],$$

$$w^{m+1} = w^m - \Delta\tau\left(c_0\partial_z + \frac{ga_z}{c_0}\right)\left(\frac{1+\beta}{2}\frac{p^{m+1}}{\rho_0 c_0} + \frac{1-\beta}{2}\frac{p^m}{\rho_0 c_0}\right) \tag{46}$$
$$+\Delta\tau\alpha_z\partial_z(\partial_x u^{m+1} + \partial_z w^m)$$
$$+\Delta\tau\frac{g(\gamma-1)}{c_0}a_z\left(\frac{c_p T^n}{c_0} - \frac{p^n}{\rho_0 c_0}\right) + \Delta\tau D_x w^{n-1},$$

$$\frac{p^{m+1}}{\rho_0 c_0} = \frac{p^m}{\rho_0 c_0} - \Delta\tau c_0\partial_x u^{m+1} \tag{47}$$
$$+\Delta\tau\left(-c_0\partial_z + \frac{g}{c_0}a_z\right)\left(\frac{1+\beta}{2}w^{m+1} + \frac{1-\beta}{2}w^m\right),$$

$$\frac{c_p T^{n+1}}{c_0} = \frac{c_p T^{n-1}}{c_0} + \frac{p^{n+1}}{\rho_0 c_0} - \frac{p^{n-1}}{\rho_0 c_0} \tag{48}$$
$$-\Delta t\left(-\frac{ga_z}{c_0}w^n - D_x\frac{p^{n-1}}{\rho_0 c_0} + D_x\frac{c_p T^{n-1}}{c_0}\right).$$

Note that with four small steps for every leap frog step, every other m-based step coincides with an n-based step, so that $m = n - 1$, $m + 2 = n$, and $m + 4 = n + 1$. The distinction between m steps and n steps in Equations (45) - (48) is retained because equal values, such as m and $n - 1$, for the step represented above, will not be equal in the subsequent small step when m is updated to $m + 1$ and $n - 1$ is held constant. Note Equations (45) - (48) are valid for any number of small time steps per big time step. These equations will be used to develop a set of equations for the specific case of four small time steps for a leap frog step.

Equations (46) and (47) are rearranged to eliminate occurences of $m + 1$ level quantities on the right hand side. Specifically, Equations (46) and (47) are solved simultaneously to eliminate w^{m+1} and $p^{m+1}/(\rho_0 c_0)$ and Equation (45) is used to replace occurences of u^{m+1}. Rewriting the u equation along with the result of the rearranged w and $p/(\rho_0 c_0)$ equations

9

gives

$$u^{m+1} = A_u^m u^m + A_w^m w^m + A_p^m \frac{p^m}{\rho_0 c_0} + A_u^{n-1} u^{n-1}, \tag{49}$$

$$w^{m+1} = B_u^m u^m + B_w^{\dot{m}} w^m + B_p^m \frac{p^m}{\rho_0 c_0} + B_p^n \frac{p^n}{\rho_0 c_0} + B_T^n \frac{p^n}{\rho_0 c_0} \tag{50}$$
$$+ B_u^{n-1} u^{n-1} + B_w^{n-1} w^{n-1},$$

$$\frac{p^{m+1}}{\rho_0 c_0} = C_u^m u^m + C_w^m w^m + C_p^m \frac{p^m}{\rho_0 c_0} + C_p^n \frac{p^n}{\rho_0 c_0} + C_T^n \frac{p^n}{\rho_0 c_0} \tag{51}$$
$$+ C_u^{n-1} u^{n-1} + C_w^{n-1} w^{n-1}.$$

Here

$$A_u^m = 1 + \tilde{\alpha}_x \tilde{\partial}_x^2, \tag{52}$$
$$A_w^m = \tilde{\alpha}_x \tilde{\partial}_x \tilde{\partial}_z, \tag{53}$$
$$A_p^m = -\tilde{\partial}_x, \quad A_u^{n-1} = \tilde{D}_x, \tag{54}$$

$$B_w^{m+1} = 1 + (\tilde{a}_z^2 - \tilde{\partial}_z^2) \left(\frac{1+\beta}{2} \right)^2, \tag{55}$$

$$B_u^m = \frac{(\tilde{a}_z + \tilde{\partial}_z) \left(\frac{1+\beta}{2} \right) (1 + \tilde{\partial}_x^2 \tilde{\alpha}_x) \tilde{\partial}_x}{B_w^{m+1}}, \tag{56}$$

$$B_w^m = \frac{1 - (\tilde{a}_z + \tilde{\partial}_z) \left(\frac{1+\beta}{2} \right) \left[(\tilde{a}_z - \tilde{\partial}_z) \left(\frac{1-\beta}{2} \right) + \tilde{\partial}_x^2 \tilde{\partial}_z \tilde{\alpha}_x \right]}{B_w^{m+1}}, \tag{57}$$

$$B_p^m = -\frac{(\tilde{a}_z + \tilde{\partial}_z) \left(1 + \frac{1+\beta}{2} \tilde{\partial}_x^2 \right)}{B_w^{m+1}}, \tag{58}$$

$$B_T^n = \frac{(\gamma - 1)\tilde{a}_z}{B_w^{m+1}}, \tag{59}$$

$$B_p^n = = -\frac{(\gamma - 1)\tilde{a}_z}{B_w^{m+1}}, \tag{60}$$

$$B_u^{n-1} = \frac{(\tilde{a}_z + \tilde{\partial}_z) \left(\frac{1+\beta}{2} \right) \tilde{\partial}_x \tilde{D}_x}{B_w^{m+1}}, \tag{61}$$

10

and

$$C_u^m = -\tilde{\partial}_x + (\tilde{a}_z - \tilde{\partial}_z)\left(\frac{1+\beta}{2}\right)B_u^m - \tilde{\partial}_x^3\tilde{\alpha}_x,$$ (62)

$$C_w^m = (\tilde{a}_z - \tilde{\partial}_z)\left(\frac{1-\beta}{2} + \frac{1+\beta}{2}B_w^m\right) - \tilde{\partial}_x^2\tilde{\partial}_z\tilde{\alpha}_x,$$ (63)

$$C_p^m = 1 + \tilde{\partial}_x^2 + (\tilde{a}_z - \tilde{\partial}_z)\frac{1+\beta}{2}B_p^m,$$ (64)

$$C_T^n = (\tilde{a}_z - \tilde{\partial}_z)\frac{1+\beta}{2}B_T^n,$$ (65)

$$C_p^n = (\tilde{a}_z - \tilde{\partial}_z)\frac{1+\beta}{2}B_p^n,$$ (66)

$$C_u^{n-1} = (\tilde{a}_z - \tilde{\partial}_z)\frac{1+\beta}{2}B_u^{n-1} - \tilde{\partial}_x\tilde{D}_x,$$ (67)

$$C_w^{n-1} = (\tilde{a}_z - \tilde{\partial}_z)\frac{1+\beta}{2}B_w^{n-1},$$ (68)

with the dimensionless quantities,

$$\tilde{a}_z = \frac{g\Delta\tau}{c_0}a_z, \quad \tilde{\partial}_x = c_0\Delta\tau\partial_x, \quad \tilde{\partial}_z = c_0\Delta\tau\partial_z, \quad \text{and} \quad \tilde{\alpha}_x = \frac{\alpha_x}{\Delta\tau c_0^2}$$ (69)

defined for convenience.

The discrete system is appended with the following equation,

$$\frac{c_pT^n}{c_0} = \frac{c_pT^{n+1}}{2c_0} + \frac{c_pT^{n-1}}{2c_0},$$ (70)

which simply averages temperature values.   Note that all the coefficients needed to describe the linearized MM5 equations are ultimately only dependent on the wave numbers k_x and k_z; the "delta's" Δx, Δz, $\Delta\tau$, and Δt; the physical constants g, c_p, and γ; the basic state parameters c_0 and ρ_0; and the pressure term averaging parameter β.

Equations (45) - (48) along with Equations (49) - (70) provide the rules for discrete time stepping for any number of small time steps per large time step. To continue the analysis we must now specify how many small time steps correspond to a leap frog time step. The standard MM5 always defaults to four small time steps per leap frog step, and this arrangement is used in our simulation experiments.   Thus, Equations (49) - (51) are written for $m + 2$, $m + 3$, and $m + 4$, by advancing the m-based variables, while leaving the n-based variables at the levels specified. For example, using Equation (50) to write the expression for w^{m+2} gives

$$w^{m+2} = B_u^{m+1}u^m + B_w^m w^{m+1} + B_p^m\frac{p^{m+1}}{\rho_0 c_0} + B_p^n\frac{p^n}{\rho_0 c_0} + B_T^n\frac{p^n}{\rho_0 c_0}$$
$$+ B_u^{n-1}u^{n-1} + B_w^{n-1}w^{n-1}.$$ (71)

11

Note that the coefficients B_u^m does not actually depend on u or m. The super- and subscripts were defined to match the variable u^m that B_u^m multiplies. This is true for all the A, B, and C coefficients.

Writing Equations (49) - (51) for the four small time steps results in twelve equations, which are combined to reduce the number of equations for u, w, and $p/(\rho_0 c_0)$ to six. Before combining equations, the levels m, $m+2$, and $m+4$ are renamed using the coinciding n-based levels, $n-1$, n, and $n+1$, respectively. The remaining m-based levels, $m+1$ and $m+3$, are eliminated using substitution. For example, in the equation for u^{m+2}, now called u^n, occurences of u^{m+1} and $p^{m+1}/(\rho_0 c_0)$ are replaced using the equations for those variables.

The six equations for u, w, and $p/(\rho_0 c_0)$ are combined with the two equations for $c_p T/c_0$, namely Equations (48) and (70), for a system of eight linear equations with eight unknowns, containing stricly n-based time levels. To write these equations compactly, let

$$\psi^n = \begin{pmatrix} u^n & w^n & \frac{p^n}{\rho_0 c_0} & \frac{c_p T^n}{c_0} \end{pmatrix}^T, \tag{72}$$

so the eight equations are

$$\psi^{n+1} = L_{11}\psi^n + L_{12}\psi^{n-1}, \tag{73}$$

$$\psi^n = L_{21}\psi^n + L_{22}\psi^{n-1}. \tag{74}$$

Note that Equation (74) is an implicit equation. Here the elements of L_{11} are

$(A_u^m)^2 + A_w^m B_u^m + A_p^m C_u^m$	$A_w^m(A_u^m + B_w^m) + A_p^m C_w^m$	$A_p^m(A_u^m + C_p^m + C_p^n) + A_w^m(B_p^m + B_p^n)$	$A_w^m B_T^n + A_p^m C_T^n$
$B_u^m(A_u^m + B_w^m) + B_p^m C_u^m$	$B_u^m A_w^m + (B_w^m)^2 + B_p^m C_w^m$	$B_u^m A_p^m + B_p^m(B_w^m + C_p^m + C_p^n) + B_p^n(B_w^m + 1)$	$B_w^m B_T^n + B_p^m C_T^n + B_T^n$
$C_u^m(A_u^m + C_p^m) + C_w^m B_u^m$	$C_u^m A_w^m + C_w^m(B_w^m + C_p^m)$	$C_u^m A_p^m + C_w^m(B_p^m + B_p^n) + C_p^m(C_p^m + C_p^n) + C_p^n$	$C_w^m B_T^n + C_T^n(C_p^m + 1)$
0	0	0	2

the elements of L_{12} are

$A_u^{n-1}(A_u^m + 1) + W_w^m B_u^{n-1} + A_p^m C_u^{n-1}$	$A_w^m B_w^{n-1} + A_p^m C_w^{n-1}$	0	0
$B_u^{n-1}(B_w^m + 1) + B_u^m A_u^{n-1} + B_p^m C_u^{n-1}$	$B_w^{n-1}(B_w^m + 1) + B_p^m C_w^{n-1}$	0	0
$C_u^{n-1}(C_p^m + 1) + C_u^m A_u^{n-1} + C_w^m B_u^{n-1}$	$C_w^{n-1}(C_p m + 1) + C_w^m B_w^{n-1}$	0	0
0	0	0	-1

the elements of L_{21} are

12

0	0	$A_w^m B_p^m + A_p^m C_p^n$	$A_w^m B_T^n + A_p^m C_T^n$
0	0	$B_w^m B_p^n + B_p^m C_p^n + B_p^n$	$B_w^m B_T^n + B_p^m C_T^n + B_T^n$
0	0	$C_w^m B_p^n + C_p^m C_p^n + C_p^n$	$C_w^m B_T^n + C_p^m C_T^n + C_T^n$
$.5(C_u^m A_u^m + C_w^m B_u^m + C_p^m C_u^m)$	$.5(C_u^m A_p^m + C_w^m B_w^m + C_p^m C_w^m - \frac{\Delta t}{\Delta \tau} a_z)$	$.5(C_u^m A_p^m + C_w^m(B_p^m + B_p^n) + C_p^m(C_p^m + C_p^n) + C_p^n)$	$.5(C_w^m B_T^n + C_p^m C_T^n + C_T^n)$

and the elements of L_{22} are

$A_u^{n-1}(A_u^m + 1) + (A_u^m)^2 + A_w^m(B_u^m + B_u^{n-1}) + A_p^m(C_u^m + C_u^{n-1})$	$A_w^m(A_w^m + B_w^m + B_w^{n-1}) + A_p^m(C_w^m + C_w^{n-1})$	$A_u^m A_p^m + A_w^m B_p^m + A_p^m C_p^m$	0
$B_u^m(A_u^m + A_u^{n-1}) + B_w^m(B_u^m + B_u^{n-1}) + B_p^m(C_u^m + C_u^{n-1}) + B_u^{n-1}$	$B_u^m A_w^m + B_w^{n-1} + B_w^m(B_w^m + B_w^{n-1}) + B_p^m(C_w^m + C_w^{n-1})$	$B_u^m A_p^m + B_w^m B_p^m + B_p^m C_p^m$	0

Now the numerical scheme is reduced into the steps in Equations (73) and (74), which can be thought of as a sequence of odd and even steps. To distinguish these steps, the levels are renamed so that

$$\psi^{2n} = L_{21}\psi^{2n} + L_{22}\psi^{2n-1}, \tag{75}$$
$$\psi^{2n+1} = L_{11}\psi^{2n} + L_{12}\psi^{2n-1}. \tag{76}$$

These equations completely describe the numerical scheme, excluding the time filter.

With the Asselin (1972) time filter, the leap frog step in Equation (76) is changed to

$$\psi^{2n+1} = L_{11}\psi^{2n} + L_{12}\overline{\psi^{2n-1}}, \tag{77}$$

where the time filter, indicated by the overbar, is given by

$$\overline{\psi^{2n}} = (1 - 2\nu)\psi^{2n} + \nu\psi^{2n+1} + \nu\overline{\psi^{2n-1}}, \tag{78}$$

with $\nu = 0.1$ as the MM5 filter constant. Combining Equations (75) and (77) gives

$$\psi^{2n+1} = L_{11}A\psi^{2n-1} + L_{12}\overline{\psi^{2n-1}}, \tag{79}$$

where, in terms of the identity matrix I,

$$A = (I - L_{21})^{-1}L_{22}, \tag{80}$$

so the scheme is completely described by (79) with the filter defined by (78).

In order to obtain a single equation for the scheme, in which filtered variables are represented in terms of unfiltered variables, the filter is applied to both sides of Equation (75), which when solved gives

$$\overline{\psi^{2n}} = A\overline{\psi^{2n-1}}, \tag{81}$$

13

using the property that $\overline{A\psi} = A\overline{\psi}$.   The filter in Equation (78) can now be rewritten as

$$A\overline{\psi^{2n-1}} = (1 - 2\nu)A\psi^{2n-1} + \nu\psi^{2n+1} + \nu\overline{\psi^{2n-1}}. \tag{82}$$

Solving for $\overline{\psi^{2n-1}}$, this gives

$$\overline{\psi^{2n-1}} = (A - I\nu)^{-1}\left[(1 - 2\nu)A\psi^{2n-1} + \nu\psi^{2n+1}\right]. \tag{83}$$

This is used to eliminate the filtered variable in Equation (79) giving the final linear evolution equation

$$\psi^{2n+1} = \mathcal{A}\psi^{2n-1} \tag{84}$$

where

$$\mathcal{A} = \left[I - \nu L_{12}(A - \nu I)^{-1}\right]^{-1}\left[L_{11}A + (1 - 2\nu)L_{12}(A - \nu I)^{-1}A\right]. \tag{85}$$

Next, it is shown how this result is used to obtain the amplitude factor and the numerical frequency. Assuming solutions of the form

$$\psi^{2n+1} = \psi_0 \exp\left(ik_x x + ik_z z\right)\exp\left(-i\omega t^{2n+1}\right), \tag{86}$$

where ψ_0 is the constant vector $(u_0 \quad w_0 \quad p_0/(\rho_0 c_0) \quad c_p T_0/c_0)^T$ that we must determine. Equation (84) can be written

$$0 = \left[\mathcal{A} - I\exp\left(-i\omega 2\Delta t\right)\right]\psi_0 \exp\left(ik_x x + ik_z z\right)\exp\left(-i\omega(t^{2n} - \Delta t)\right), \tag{87}$$
$$0 = \left[\mathcal{A} - I\lambda\right]\psi^{2n-1}, \tag{88}$$

using $\lambda = \exp\left(-i\omega 2\Delta t\right)$. Nontrivial solutions for ψ^{2n-1} exist for

$$\det\left(\mathcal{A} - I\lambda\right) = 0, \tag{89}$$

which leads to four eigenvalues (values for λ), from which the appropriate value for the gravity wave of interest is selected, as discussed below. Each eigenmode then simply evolves according to

$$\psi^{2n+1} = \lambda\psi^{2n-1}, \tag{90}$$

that describes the effect of the numerical scheme. The amplitude and frequency information are contained in the real and imaginary parts of λ, or in terms of frequency, they come from

$$\lambda = \exp\left(-i(\omega_r + i\omega_i)2\Delta t\right) = \exp\left(-i\omega_r 2\Delta t\right)\exp\left(\omega_i 2\Delta t\right). \tag{91}$$

So over a leap frog step, the amplitude of the gravity wave of interest is adjusted by a factor of

$$|\lambda| = \exp\left(\omega_i 2\Delta t\right) = \text{Re}(\lambda) \tag{92}$$

and the numerical frequency of the wave is

$$\omega_n = \text{Re}(\frac{i\log\lambda}{2\Delta t}). \tag{93}$$

14

k_x, k_z	ω	C_p	C_g
(+,+)	+	(+,+)	(+,-)
(+,+)	-	(-,-)	(-,+)
(+,-)	+	(+,-)	(+,+)
(+,-)	-	(-,+)	(-,-)
(-,+)	+	(-,+)	(-,-)
(-,+)	-	(+,-)	(+,+)
(-,-)	+	(-,-)	(-,+)
(-,-)	-	(+,+)	(+,-)

Table 1: Association between frequency sign and gravity wave travel direction. Here $C-g$ is the group velocity and C_p is the phase speed.

Solving Equation (89) leads to four eigenvalues, from which the one associated with an upward-traveling gravity wave is selected. The selection is based on the magnitude and sign of the frequency. Two eigenvalues lead to high frequencies, on the order of 0.08 s^{-1}, which imply oscillation periods on the order of 1.3 minutes. These frequencies are higher than the Brunt Väisälä frequency of $0.012 s^{-1}$ and are therefore discarded as describing gravity waves. The other two eigenvalues lead to frequencies on the order of 0.0008 s^{-1}, which imply oscillation periods on the order of 140 minutes, which are consistent with gravity waves. This leaves two gravity wave eigenvalues, which are opposite in sign and nearly equal in magnitude. These are the two beams of the cross.

The dispersion relation and group speed from the idealized case, given in Equations (16) - (18), can be used as a guide to associating frequency sign with gravity wave direction of travel. For example, if the wavenumber (k_x, k_z) signs are (+,-) and the frequency (ω) is positive, then the group speed vector (C_g) has signs (+,+). The other combinations are given in Table 1 for use in interpreting calculations in association with the numerical analysis as described in the following sections.

Numerical dissipation is typically quantified in terms of the order r in $A = 1 - Cf^r$, where C is a constant, and f depends on grid and wave parameters (Strikwerda 1989). In the current problem f is not readily determined and therefore the quantity $\mathcal{D}$, which varies like $r \ln f$, is used. The amplification factor is related to $\mathcal{D}$ by

$$\ln(1 - A_a) = \mathcal{D}_a + B_a, \qquad (94)$$

where $A_a = A_V^{(4)}$, B_a is a constant, and the subscript a refers to results based on analysis. The constant B_a is combined with its counterpart for experimental dissipation as discussed in Section 5.
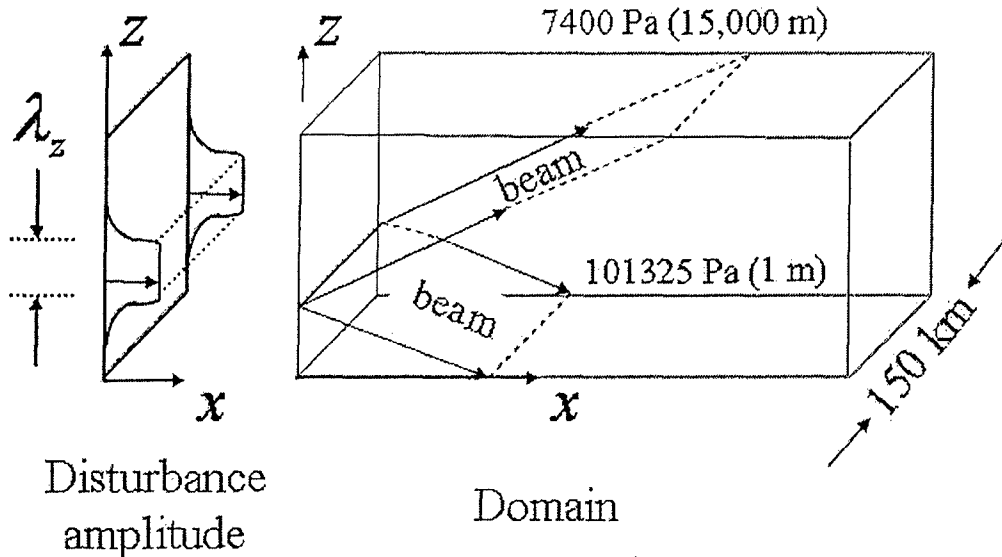
15

Figure 1: MM5 domain and boundary disturbance.

4 Numerical Experiment

The MM5 is implemented for an idealized atmosphere for eight sets of grid and wave parameters. Simulations are in a single domain without moisture, Coriolis effects, a planetary boundary layer, or tropopause. The terrain is uniform and the background state of the atmosphere is given by an ideal gas in hydrostatic balance with no flow and a temperature profile of the standard atmosphere (Holton 1992), resulting in a nearly uniform Brunt Väisälä frequency of $0.012 s^{-1}$. Such conditions should be steady, but because of boundary conditions and the effects of descretization the specified state is not exactly steady. Therefore a preliminary forecast is run with constant boundary conditions to allow the model to make any small adjustments required to reach a steady state.

A two-dimensional disturbance, satisfying the gravity-wave solution in (11) - (15) is introduced at one lateral boundary, approximately centered in the model vertical domain. The disturbance has a vertical extent equal to one vertical wavelength, above and below which the disturbance decays as shown in Figure 1. The other three lateral boundaries have no-flow conditions. In order to simulate the two-dimensional problem in a three-dimensional atmosphere, the disturbance is applied uniformly across the third dimension (the N-S or y dimension in MM5 notation).

The resulting flow contains an upward-traveling beam and a downward-traveling beam, forming the right half of St. Andrew's Cross. Once the beams have developed, cross sections involving the N-S dimension are examined to confirm qualitatively that the flow is uniform in the N-S dimension, indicating two-dimensional flow. Cross sections showing half of the X-pattern are examined at several times to confirm that wave quantities, including wave
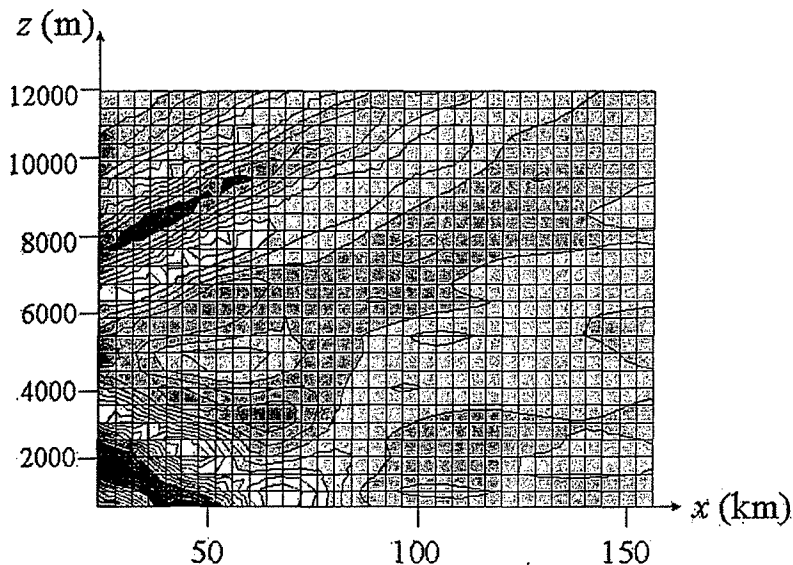
16

Figure 2: Example of MM5 gravity-wave response as shown in a cross-section of the perturbation density field.

numbers, frequencies, beam angle, and group and phase velocities, are consistent with theory.

Reflections from the top of the domain are observed and found to interfere eventually with the waves of interest. To exclude the influence of these reflections, a final time is selected for each wavenumber so there is sufficient time for beams to form, yet not enough time for reflections to have a noticeable influence. Beam-center velocities in upper beams are measured from MM5 data and combined with the known background density to obtain beam-center amplitudes used in dissipation evaluations.

Theoretical, numerical, and practical considerations limit the range of wave numbers used. Scales consistent with typical MM5 use are adopted so that $\Delta x \gg \Delta z$. As noted by Leutbecher and Volkert (2000), using a wavelength of two horizontal grid cells would result in large errors, due to the artificial dissipation, which is designed to suppress such waves. Therefore wavelengths are selected so that at least four horizontal grid cells represent a wave. The vertical wavelength must be large enough to be well resolved on the given grid and small enough so that waves do not span large changes in background density as required by (19) for the calculation of C_g. For the atmosphere used, this is equivalent to an upper bound on the vertical wavelength of about 6000 m. In practice, the vertical wavelength is kept well below this limit to maximize the time until reflections from the upper and lower boundaries interfere with the analysis. For convenience, waves are also selected on the basis of beam angles and wave periods.

An example of a beam that has developed but has not yet been influenced by boundary effects is shown as a cross-section of the perturbation density field in Figure 2. Such images are reviewed at different stages of beam evolution to confirm the flow is two-dimensional,

Case	Horizontal spacing (m)	Vertical spacing (m)	k_x	period (min)	C_{gz}/C_{gx}
1	3000	434	.000265	60	.11
2	3000	217	.000228	60	.13
3	2500	434	.00024	60	.13
4	2700	217	.00027	60	.12
5	3000	434	.000154	120	.053
6	3000	217	.00013	120	.065
7	2500	434	.000174	120	.072
8	2700	217	.000134	120	.064

Table 2: MM5 grid spacing and waves.

not impacted by boundary reflections, and that the waves satisfy the dispersion relation.

The eight MM5 cases are summarized in Table 2. The cases represent waves with either a 60-minute period or with a 120-minute period, simulated by four different grids. The waves are subject to filtering at the boundary as they enter as well as to numerical dissipation as they propagate. Therefore, input wave parameters may differ from observed parameters in the MM5 results. For calculation purposes, two observable wave parameters are taken from these results to characterize the waves. The wave period observed was consistent with its input value, so this was used as one parameter. For the other parameter, the horizontal wave number, k_x was used, since it could be measured in a consistent way from case to case, using images like the one in Figure 2.

The vertical wave number is calculated using the numerical dispersion relation. This was accomplished using the forward problem that solves for frequency, or period, and decay rate ($|\lambda|$), given horizontal and vertical wave number and grid parameters. The procedure was applied repeatedly to obtain the inverse, that is to obtain the vertical wave number, given the horizontal wave number and the frequency. The results are shown in Table 3, along with the decay rate and the slope of the group velocity for each of the eight cases based on the numerical analysis.

5   Results

The beams produced for the eight cases are evaluated both in the context of dissipation associated with viscous theory and dissipation expected based on numerical analysis. Viscous theory provides a gauge for the levels of dissipation observed in the numerical experiments. Numerical analysis provides a means to predict how numerical dissipation varies with wave and grid parameters.

For comparison to viscous theory, MM5 beam amplitudes as a function of the beam-

Case	k_z	$|\lambda|$	C_{gz}/C_{gx}
1	-.00120	.9968	.24
2	-.00106	.9982	.22
3	-.00110	.990	.23
4	-.00250	.9978	.23
5	-.000154	.9996	.086
6	-.00124	.9998	.11
7	-.00161	.9997	.12
8	-.00128	.9998	.11

Table 3: Calculated wave parameters based on numerical analysis

following coordinate ξ, are fit to the function

$$V(\xi)\sqrt{\rho_0(\xi)} = V(\xi_0)\sqrt{\rho_0(\xi_0)}\left(\frac{\xi}{\xi_0}\right)^{-F}, \tag{95}$$

to find the exponent F. The value of F is compared to the the value 2/3 from (22) to indicate the MM5 level of damping relative to theoretical, viscous damping. An example of amplitude along a beam is shown in Figure 3 for case 3 (from Table 3), with markers to indicate MM5 values, a solid curve to show the best-fit function for those values, and a dashed line to show theory. In this example, MM5 amplitude decreased faster than the theoretical prediction for a beam in a viscous fluid. The oscillations in the MM5 values are largely due to the beam center following a staircase pattern through the MM5 grid.

A summary of F values for all eight cases is shown in Figure 4. This shows that for cases 1 - 4, MM5 damping is greater than theoretical viscous damping, while for the remainder it is less. This suggests that in cases where $k_x\Delta_x > .55$, or when fewer than about eleven horizontal grid cells represent a wave, MM5 numerical dissipation is stronger than what would be expected due to molecular viscosity, while in cases with more than about eleven horizontal grid cells per wave, it is weaker. Numerical analysis of dissipation is used to extend results over a range of waves and grids.

In order to show that numerical dissipation analysis does in fact describe MM5 performance, the two are compared. First, the results of the numerical experiment are quantified in terms of amplification factor, which leads to dissipation value. The experimental amplification factor is based on fluid speeds observed along a beam, $V(\xi)$. Values of $V(\xi)$ at a fixed time are interpreted as equivalent local speeds at different times. For example, losses over the period Δt, when waves travel from ξ_0 to ξ_1, are given by the amplification factor

$$(A_V)^N = \frac{V(\xi_1)\sqrt{\rho_0(\xi_1)}}{V(\xi_0)\sqrt{\rho_0(\xi_0)}}, \tag{96}$$

where $N = (\xi_1 - \xi_0)/(C_g\Delta t)$ is the number of large time steps. In this formulation the square root of density is included because $V\sqrt{\rho_0}$ is conserved along a compressible, inviscid beam.
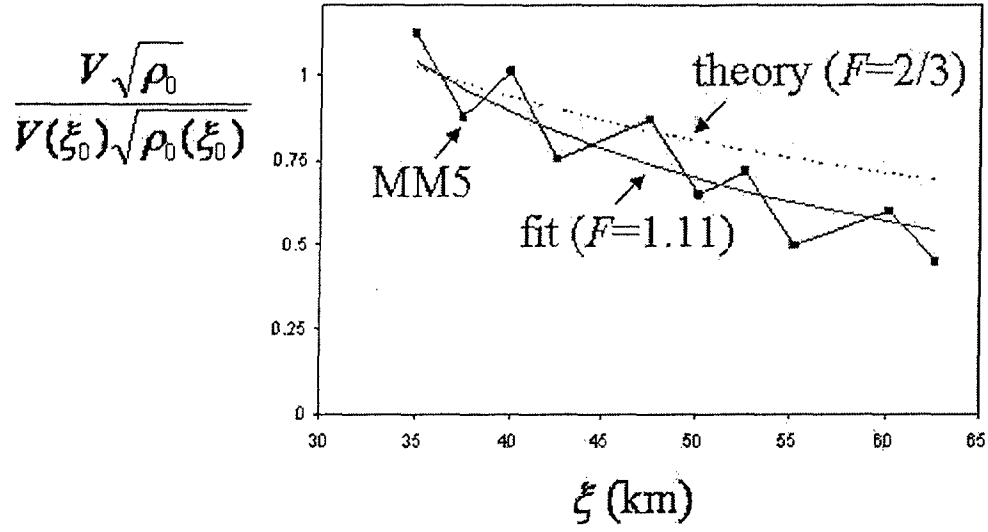
Figure 3: Amplitude along a beam from MM5 at a single time, best fit curve, and theory based on case 3 in Table 3.
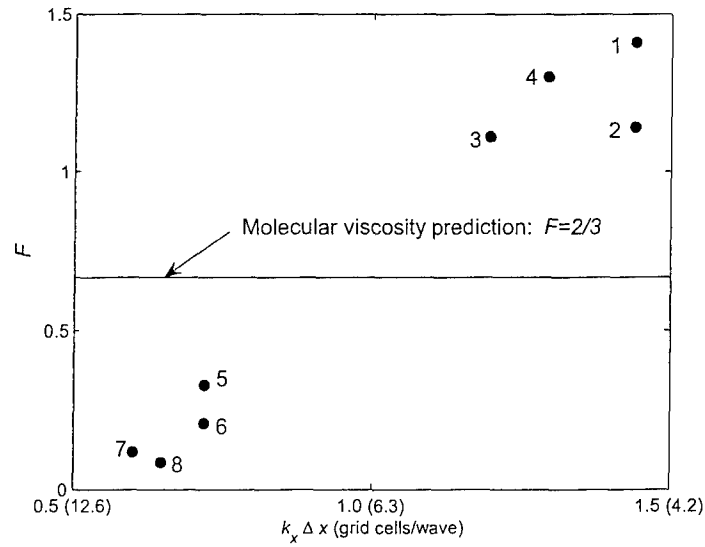

Figure 4: Beam amplitude loss in terms of F for the eight numerical experiment cases, along with theoretical value, $F = 2/3$.
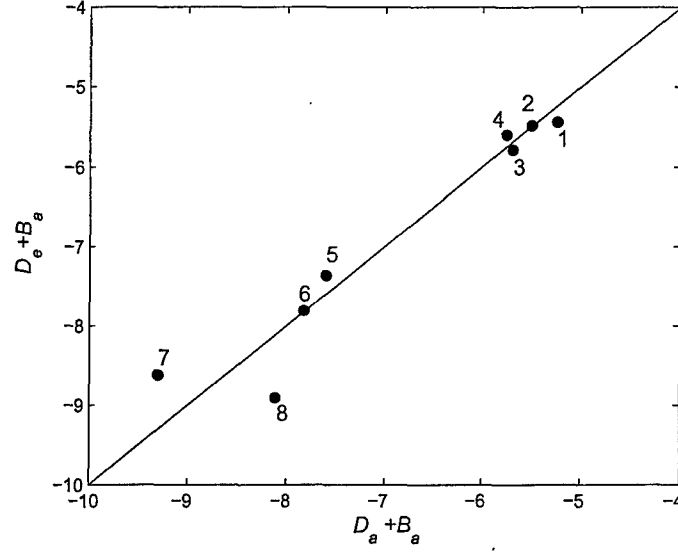
Figure 5: Comparison of experimental dissipation ($\mathcal{D}_e + B_a$) with dissipation predicted by analysis ($\mathcal{D}_a + B_a$) for the eight numerical experiment cases.

The amplification factor due to numerical experiment, A_e, is computed as the least squares fit value for A_V to all beam positions from a single, upper beam. Typically, ten to twenty grid points along a beam are available, depending on grid spacing and other parameters.

Following the form of the dissipation according to analysis given by Equation (94), a provisional dissipation value based on experiment is $\ln(1 - A_e)$. This can be written as the sum of a constant and a term proportional to the order of dissipation, denoted $\mathcal{D}_e$. To unify the constants added to $\mathcal{D}_e$ and $\mathcal{D}_a$, the average difference between the constants is used as an adjustment term, assuming $\mathcal{D}_a$ approximates $\mathcal{D}_e$. The final form for the experimental dissipation value is

$$\mathcal{D}_e + B_a = \ln(1 - A_e) - \left(\overline{\ln(1 - A_e)} - \overline{\ln(1 - A_a)} \right), \tag{97}$$

where the bars indicate averages over the eight cases studied.

The experimental dissipation, $\mathcal{D}_e + B_a$, is compared to calculations of $\mathcal{D}_a + B_a$ for the eight simulated beams in Figure 5, using case numbers from Table 2 as markers. The diagonal line indicates perfect agreement between analysis and experiment, with the amount of dissipation increasing toward the top right of the diagonal. Markers are close to the line, indicating the analysis is an approximate predictor of numerical dissipation. The agreement between experiment and analysis shown in Figure 5 allows for conclusions that apply beyond the experimental cases, using the numerical dissipation analysis in a limited range of parameters.

The results on Figure 5 form two clusters: an upper cluster of the short-wave cases numbered 1 - 4 and the lower cluster of the long-wave cases numbered 5 - 8. Of the two clusters the short-wave cluster has greater numerical dissipation as indicated by its higher
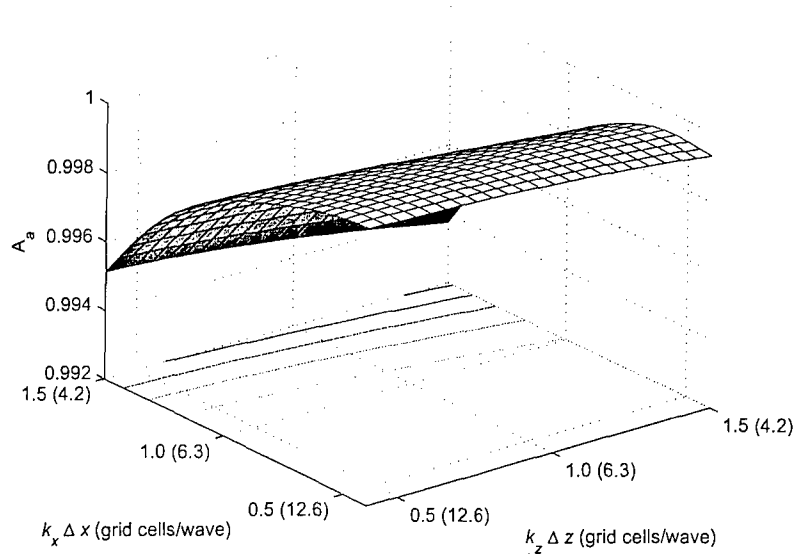
21

Figure 6: Beam amplitude predicted by analysis for a range of horizontal and vertical parameters.

position on the diagonal. This is consistent with Figure 4 in which the short-wave cases are shown to contain greater dissipation than the long-wave cases. Given that the short and long waves differ by a factor of two, while the horizontal grids differ by only about ten percent, it is not surprising that results are partitioned by wavelength and not horizontal grid spacing. However, the vertical grid spacings differ by a factor of two, but do not produce anywhere near the impact of the same factor when applied to horizontal wavelength. For example, cases 1 and 2, between which vertical grid spacing differs by a factor of two, show little difference in dissipation in comparison to the dissipation difference between cases 1 and 5, which reflect a factor-of-two difference in horizontal wavelength. The same observation can be made with other pairings of the data in Figure 5. This confirms the importance of horizontal grid spacing noted earlier by Leutbecher and Volkert (2000).

Figure 6 shows the predicted amplitude based on the amplification factor determined by the numerical analysis of Section 3. Figure 6 shows that amplitude increases, or equivalently dissipation decreases, as either $k_x \Delta x$ or $k_z \Delta z$ decreases. In other words numerical dissipation decreases with refined resolution of waves. The dissipation is so much more sensitive to horizontal refinement than vertical refinement is evidenced by the shape of the surface in Figure 6. The values $(k_x, k_z) = (0.00036, -0.0033)$ are used for the figure, with ω satisfying the dispersion relation and $\Delta\tau = 3\Delta x/1000$. Similar results are found for other wavenumber pairs.

22

6 Conclusions

Idealized experiments demonstrate that MM5 simulation of gravity-wave beam propagation is consistent with theoretical predictions of speed and direction. MM5 beams lose amplitude due to numerical dissipation. Using molecular viscosity as a gauge, the numerical dissipation can be greater or less than viscous dissipation predicted for a compressible atmosphere, depending on the grid resolution and wave parameters.

As expected, improving the resolution of the wave in either the horizontal or vertical generally decreases numerical dissipation. Both numerical analysis and numerical experiment show greater sensitivity to horizontal resolution than vertical, reflecting the influence of the horizontally-based artificial dissipation.

Due to the relative sensitivity to horizontal spacing, as compared to vertical spacing, the horizontal spacing alone can be used to approximately predict numerical dissipation. The amount of numerical dissipation for a wave represented by eleven horizontal grid cells is approximately equivalent to the amount of dissipation that would be imposed if molecular viscosity were present. Numerical dissipation is greater than this amount if the wave is resolved by fewer horizontal cells, and less than this amount if more horizontal resolution is used.

These results could be used to better understand MM5 results and as a consideration in selecting grids. This approach establishes a way to perform idealized numerical experiments that can be applied to other models for model investigation or to compare different models on the basis of their core calculations as opposed to their parameterizations or boundary conditions.

Further work is in order to make use of the predictions of numerical analysis in terms of wave quantities.

References

Asselin, R. (1972). Frequency filter for time integrations. *Mon. Wea. Rev. 100*(6), 487–490.

Dewan, E. M., R. E. Good, R. Beland, and J. Brown (1993). *A Model for C_n^2 Profiles Using Radiosonde Data*. Phillips Laboratory Tech Report PL-TR-93-2043, Hanscom AFB, MA, 42 pp.

Dudhia, J. (1993). A nonhydrostatic version of the Penn State-NCAR mesoscale model: Validation tests and simulation of an Atlantic cyclone and cold front. *Mon. Wea. Rev. 121*(5), 1493–1513.

Durran, D. R. (1991). The third-order Adams-Bashforth method: An attractive alternative to leapfrog time differencing. *Mon. Wea. Rev. 119*(2), 702–720.

Grell, G. A., J. Dudhia, and D. R. Stauffer (1994). *A Description of the Fifth-Generation Penn State/NCAR Mesoscale Model (MM5)*. NCAR Tech Note NCAR/TN-398+STR, 122 pp.

Holton, J. R. (1992). *An Introduction to Dynamic Meteorology*. New York: Academic Press, 486 – 487.

Leutbecher, M. and H. Volkert (2000). The propagation of mountain waves into the stratosphere: Quantitative evaluation of three-dimensional simulations. *J. Atmos. Sci. 57*, 3090 – 3108.

Lighthill, M. J. (1978). *Waves in Fluids*. Cambridge University Press, 284 – 298.

Mowbray, D. E. and B. S. H. Rarity (1967). A theoretical and experimental investigation of the phase configuration of internal waves of small amplitude in a density stratified liquid. *J. Fluid Mech. 28*, 1 –16.

Ruggiero, F. H., D. A. DeBenedictis, R. J. Lefevre, and S. A. Early (2004). Mesoscale modeling effects on optical turbulence parameterization performance. In *20th Conference on Weather Analysis and Forecasting, 116th Conference on Numerical Weather Prediction*, Seattle.

Strikwerda, J. C. (1989). *Finite Difference Schemes and Partial Differential Equations*. Pacific Grove: Wadsworth and Brooks/Cole, 386 pp.

Tabaei, A. and T. R. Akylas (2003). Nonlinear internal gravity wave beams. *J. Fluid Mech. 482*, 141 – 161.

Thomas, N. H. and T. N. Stevenson (1972). A similarity solution for viscous internal waves. *J. Fluid Mech. 54*, 495 – 506.